Soft Matter

RSC Publishing

PAPER

View Article Online
View Journal | View Issue

Cite this: *Soft Matter*, 2013, **9**, 7049

Control and manipulation of microfluidic flow *via* elastic deformations

Douglas P. Holmes,*[a] Behrouz Tavakol,[a] Guillaume Froehlicher[b] and Howard A. Stone[b]

Received 11th April 2013
Accepted 29th April 2013

DOI: 10.1039/c3sm51002f

www.rsc.org/softmatter

We utilize elastic deformations *via* mechanical actuation to control and direct fluid flow within a flexible microfluidic device. The device consists of a microchannel with a flexible arch prepared by the buckling of a thin elastic film. The deflection of the arch can be predicted and controlled using the classical theory of Euler buckling. The fluid flow rate is then controlled by coupling the elastic deformation of the arch to the gap within the microchannel, and the results compared well with analytical predictions from a perturbation calculation and numerical simulations. We demonstrate that placement of these flexible valves in series enables directed flow towards regions of externally applied mechanical stress. The simplicity of the experimental approach provides a general design for advanced functionality in portable microfluidics, self-healing devices, and *in situ* diagnostics.

Introduction

Fluid flow within flexible geometries occurs in many biological environments, and its characteristics are determined by a balance of fluid properties, pressure, and structural deformation.[1,2] This balance is important in poroelastic materials, where the pressure gradient in the fluid is often the consequence of an externally applied stress causing the fluid to interact with the elastic network and move away from the external force.[3] Some biological systems function to regulate fluid flow within confined geometries using passively activated internal valves. For example, as a giraffe changes its posture from standing to drinking, a pressure-regulated collapse of its jugular vein maintains an adequate internal blood pressure and flow rate.[2,4] Biological fluid flow can also be directed towards regions of high mechanical stress, as observed in the porous microstructure of bone, where mechanical strain can induce mechanotransduction for rheotaxis.[5–7] We present a material with internal flexible valves that can control and direct fluid flow *via* external mechanical actuation for use in advanced materials for *in situ* mixing, chemical reactions, and rapid, portable chemical analysis. In particular, we microfabricate internal flexible valves so that macroscopic deformation leads to valve function that regulates fluid flow and so can direct flow from low to high regions of external stress. Creating a bio-inspired method for internal flow regulation will be useful for controlling fluid flow within multifunctional devices.[8]

Porous elastic gels and microstructured fluid channels have been used to control flow in many soft material settings,[8] and these fluid networks can approach the complexity found in integrated circuits.[9–11] Fluid transport can be driven actively using external macroscale pumps, pressure or vacuum chambers, and electrical signals,[12,13] or passively *via* surface tension[14] and swelling.[15,16] While significant advances in controlling fluid flow continue to be made using externally actuated valves, the presence of external power and hardware limit a device's range of use.[17] The development of a fully internally controlled device will enable portable or embeddable devices for controlling and manipulating flow, for example, within self-healing and self-strengthening materials.

In this paper, we utilize elastic deformations within a flexible device, driven by mechanical actuation, to control and direct fluid flow internal to a soft material. In particular, a fluid confined to one compartment of a channel will flow through a channel when a pressure drop is created by stretching or bending the material (Fig. 1). The basis of our approach is a flexible arch within a milli- or microfluidic channel, which is designed to prevent fluid flow in its initial, strain-free state. Upon deforming the device, the arch's curvature decreases and acts like a valve allowing fluid to flow. The design represents a fluid-control analogue to the use of a buckled conducting wire in the design of flexible electronic devices.[18,19] We use a mathematical model based on the buckling of an Euler column to predict the deformation of the arch and a perturbation analysis based upon lubrication theory to predict the corresponding flow rate within the channel for varying degrees of arch deformation. By extending this design to include multiple arches within a channel, we illustrate how local material deformations will cause fluid flow towards a region of high applied stress, which,

[a]*Department of Engineering Science & Mechanics, Virginia Tech, Blacksburg, VA, USA. E-mail: dpholmes@vt.edu; Tel: +1 540 231 7814*

[b]*Department of Mechanical & Aerospace Engineering, Princeton University, Princeton, NJ 08544, USA*

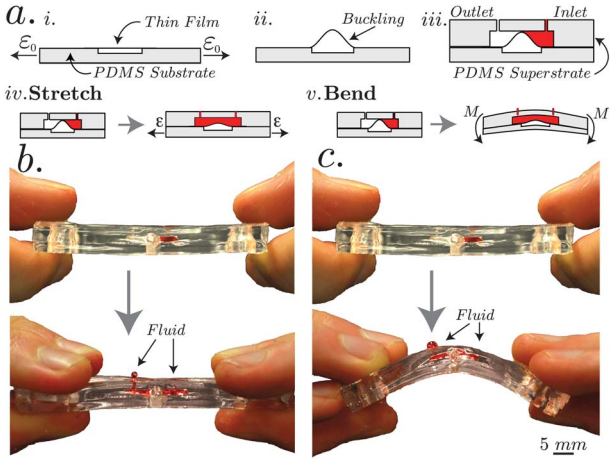

Fig. 1 (a) Schematics illustrating the fabrication and functionality of a device with an internal flexible valve. (i) The substrate is stretched and then a thin film is bonded to it. (ii) Upon releasing the initial strain, the thin film buckles to an arch, and (iii) the substrate is fabricated into a microfluidic device, and the arch closes the channel. Applying an external mechanical loads such as (iv) stretching and (v) bending, partially opens the valve and allows fluid flow. (b and c) Images of the fabricated device that allows the fluid flow upon stretching and bending.

with appropriate choice of liquids, can serve as the basis for self-healing and active-sensing materials, as well as metamaterials capable of exhibiting "negative" poroelastic fluid flow.

Model: flexible valve

To develop the general construct for an internally controlled fluid flow device, we first consider the fabrication of a mechanically actuated valve, after which we determine a relationship between the geometry of the channel, the pressure drop, and the fluid flow rate. For the mechanically controlled valve, a thin elastomeric film is partially bonded to a uniaxially strained elastic substrate (Fig. 1a-i). Release of the strain on the substrate induces a uniaxial compressive strain ε_0, which buckles the thin film into an arch with a deflection w_0 at its center (Fig. 1a-ii). If we consider the symmetric buckling of a beam, the profile of the thin film will adopt a cosine shape,[20] such that the arch height along its length is $\tilde{w}(x) = \frac{w(x)}{L_0} = \frac{1}{\pi}\sqrt{\varepsilon_0(\varepsilon_0 - 1)}\left(1 + \cos\frac{2\pi x}{L_0}\right)$, where L_0 is the original length of the beam (Fig. 2a). Therefore, after fabrication the height of the arch at its center, $w_0 = \tilde{w}(0)$, is:

$$\frac{w_0}{L_0} = \frac{2}{\pi}\sqrt{\varepsilon_0(\varepsilon_0 - 1)}. \quad (1)$$

To confirm this relation, the arch height after fabrication w_0 was measured as a function of compressive strain ε_0, and we found good agreement between theory and our experimental results (Fig. 2b).

With an accurate model of the arch height, we prepared a superstrate with a channel height $W = w_0$ for a specific ε_0, and bonded it to the flexible device substrate (Fig. 1a-iii), such that the minimum gap height within the channel is initially $b = 0$. Since the arch is deformable, uniaxial tension from stretching

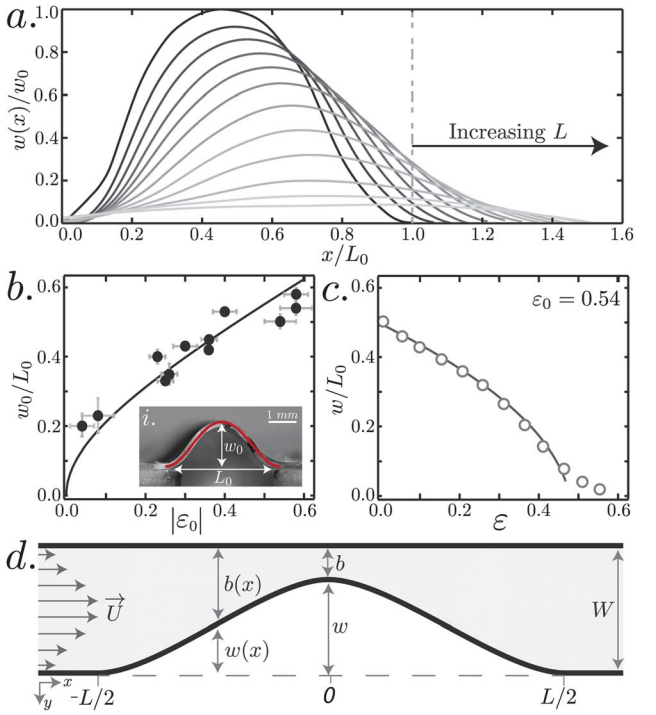

Fig. 2 (a) Experimentally measured profiles† of buckled thin films as each structure is stretched from its initial length $L_0 = 1.2$ mm to a new length L. (b) The initial deflection of the center of the arch w_0/L_0 after fabrication is plotted as a function of the strain and eqn (1), and the inset (i) shows the cross section of an arch overlaid with the theoretical curve. (c) The height of the arch at its center w/L is plotted as a function of strain with eqn (2) and the identity $W = w + b$. (d) A schematic of fluid flow within the microfluidic device. A fluid with velocity $\vec{U}$ flows from $-L/2$ to $L/2$ over an elastic arch with the shape $w(x)$. The height of the gap is described by the compliment of the arch's height, $b(x)$, that spans the channel height W.

(Fig. 1b) or bending (Fig. 1c) the material by a strain ε will increase $L > L_0$, thereby decreasing the arch height $w = \tilde{w}(0)$, and increasing the gap height within the channel (Fig. 2a). To develop a relationship between the channel geometry and mechanical strain, it is convenient to rewrite eqn (1) in terms of the gap between arch's center and the top wall $b = W - w$, where w and b are the maximum arch height and minimum gap height for a given strain ε, respectively. By neglecting higher-order terms in ε, the minimum gap within the channel is:

$$\frac{b}{W} = 1 - \frac{2}{\pi}\frac{L_0}{W}\sqrt{\left(\frac{\pi}{2}\frac{w_0}{L_0}\right)^2 - \varepsilon}. \quad (2)$$

Fig. 2c shows the change in arch height at its center as a function of uniaxially applied strain. The theoretical line is in good agreement with our experimental results.

Model: fluid flow

From eqn (2), we know the geometry within the channel as an applied uniaxial strain ε causes the gap to go from closed, $b/W = 0$, to open, $b/W = 1$ (Fig. 2d). Using this relationship between ε and b, we can now determine by a perturbation calculation the

† Experimental profiles have to be shifted so that the maximum of the profile occurs at $x = 0$ to compare with $\tilde{w}(x)$.

flow rate Q through the channel for a given pressure drop ΔP. We consider a two-dimensional flow in a rectangular channel, with a flow rate $Q_c = \frac{W^3 \Delta P}{12 \mu L}$, and assume that the aspect ratio $\delta = b/L$ and the Reynolds number $\mathscr{R} = \rho b u_c/\mu$ satisfy $\delta \ll 1$ and $\mathscr{R}\delta \ll 1$, where $u_c = \frac{Q_c}{b}$ is the characteristic fluid velocity, μ is the fluid viscosity, and ρ is the fluid density. We have solved this problem numerically and also developed analytical approximations useful for prediction and design. From the momentum balance, we have two differential equations for the pressure change in the x and y directions, such that, in dimensionless form, $\partial_x p = \partial_{yy}{}^2 u + \delta^2 \partial_{xx}{}^2 u$ and $\partial_y p = \delta^2 \partial_{yy}{}^2 v + \delta^4 \partial_{xx}{}^2 v$, where x is normalized by the length L_0, and y is normalized by the width W. In these equations, δ only exists as even powers, suggesting that the dimensionless velocities $u = \frac{U}{q_0/W}$, $v = \frac{V}{q_0/L_0}$, and dimensionless pressure $p = \frac{Pb^2}{\mu u_c L}$ can be determined by a series expansion in even powers of δ, *e.g.* $u(x,y) = \sum_{n=0}^{\infty} \delta^{2n} u_{2n}$.‡ We assume no-slip boundary conditions along the walls and along the arch, and at zeroth order, we obtain:

$$\Delta p_0 = \frac{3(8 - 8\lambda + 3\lambda^2)}{(1-\lambda)^{5/2}}, \tag{3}$$

where $\lambda = 1 - \frac{b}{W}$. By replacing u_0 and p_0 into the equations for the momentum balance at the second order and solving for the velocities u_2, and v_2, we determine for the pressure drop at the second order,

$$\Delta p_2 = \frac{12\pi^2 \lambda^2}{5(1-\lambda)^{3/2}}. \tag{4}$$

The fourth-order term, Δp_4, can be determined in the same manner.§ With the normalized pressure drop at each order of the expansion, we can return these terms to dimensional quantities by knowing the gap within the channel, and calculate the total pressure drop $\Delta P = \sum_{n=0}^{\infty} \delta^{2n} \Delta P_{2n}$.

Results and discussion

Using the total pressure drop and normalizing it by the pressure drop in an empty rectangular channel, $\Delta P_c = 12\mu Q_c L W^{-3}$, we can calculate the flow rate $Q = \sum_{n=0}^{\infty} \delta^{2n} Q_{2n}$ normalized by the flow rate in an empty channel Q_c. To confirm this perturbation calculation experimentally, we applied a constant pressure between the inlet and outlet of the device, and measured the flow rate at the outlet. In addition to the experimental study, we used computational analysis to verify the analytical solution. We performed numerical simulations across the entire range of microfluidic gap heights (Fig. 3a). The theory, numerical simulations, and experimental results are plotted in Fig. 3b and are in very good agreement. The higher-order expansions

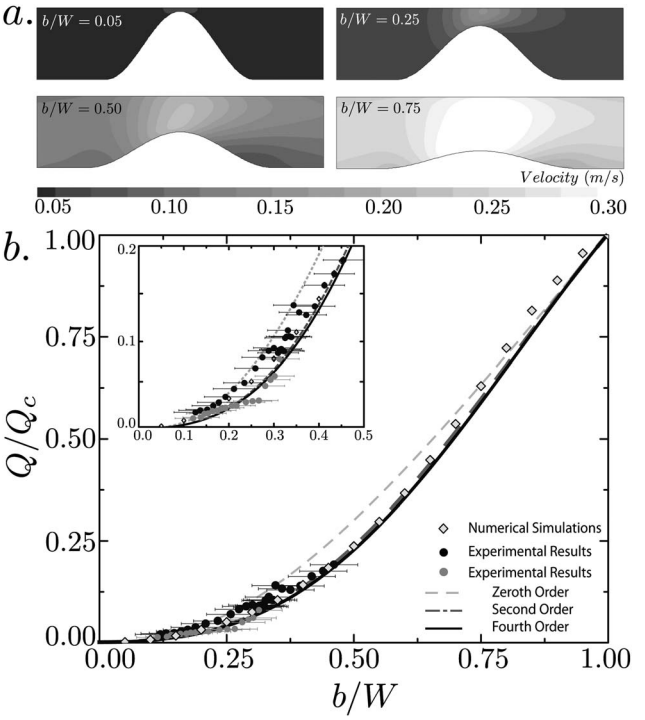

Fig. 3 (a) Numerical simulations of pressure-driven flow for several channels with different gap heights b/W. Refer to the materials and methods for the specific parameters used in these simulations. (b) The flow rate Q normalized by the two-dimensional flow in a rectangular channel Q_c and plotted *versus* b/W. The solid lines represent the zeroth, second, and fourth order solutions to the perturbation approach in lubrication theory.

appear to better describe the fluid flow as the gap between the arch and the wall increases. In this way, we can now predict the magnitude of internal flow within the deformed microstructured material for a given applied internal pressure difference and a given opening of the arch.

The above experiments and model provide an approach to have external mechanical stresses induce internal fluid flow. A primary advantage to this design is that more complex microfluidic architecture leads to advanced functionality. Internally structured materials often exhibit unexpected mechanical behavior, such as the strength and stiffness of cellular solids,[21,22] and the negative Poisson behavior[23] of foams[24] and periodically microstructured materials.[25,26] We demonstrate the ability to direct fluid flow towards regions of high mechanical stress by preparing two arches in series and applying a high pressure in the channel between them (Fig. 4a). Both valves are initially closed and the applied fluid pressure in the middle cannot cause the valves to open, *i.e.* the pressure is not high enough to deform the valves; otherwise, the system may behave differently. With this configuration, locally applied mechanical stress to one end of the device, in this case the right side, will cause one arch to deform, *i.e.* $b/W > 0$, creating a pressure gradient in the direction of the mechanically applied load. Therefore, opening of a single valve, as seen experimentally and numerically in Fig. 4a–c, causes fluid flow from left to right, in the direction of the applied load. It should be noted that

‡ The mathematics of the derivation will be published as a separate part of the analysis of fluid motion in these systems.

§ $\Delta p_4 = \frac{8\pi^4[-428(-1+\sqrt{1-\lambda}) + 214(-2+\sqrt{1-\lambda})\lambda + 53\lambda^2]}{175\sqrt{1-\lambda}}$.

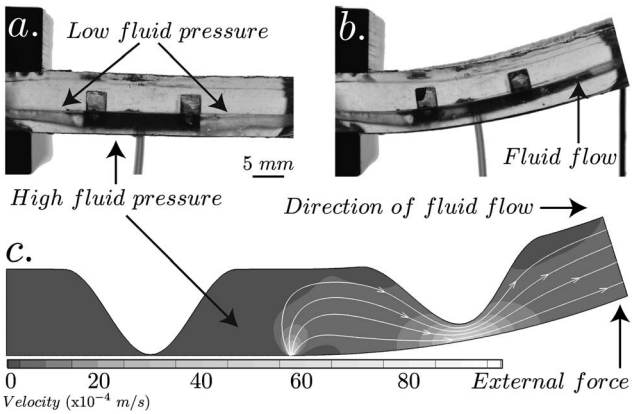

Fig. 4 (a) A microfluidic device with two flexible arches in series is clamped at one end and a line load applied to the opposite end. (b) The localized deformation causes the arch closest to the applied load to deform and allow fluid to flow towards the region of high stress. (c) A numerical simulation of the multichannel arch illustrates the directed fluid flow.

without these internal valves, the fluid can go to either sides since we have high fluid pressure in the middle and low fluid pressure in both sides. Therefore, the fluid pressure only helps to have flow but the direction of the flow is determined by the externally mechanical stress. In this simple demonstration, the fluid flows from regions of high fluid pressure to low fluid pressure, yet because of the material's internal microstructure, this pressure drop occurs in the direction of the externally applied mechanical stress.

It is clear that a wide variety of functionality can be attained when the flexible microfluidic architecture is increased in complexity. Internally directing fluid flow with these structural valves provides compelling opportunities for moving fluid within microstructured materials. For example, embedding multiple arrays of flexible valves and microchannels within a porous material will enable external loads to move fluid in a gradient controlled by the internal microstructure. Structuring the porosity of a material, and therefore the deformation of its microstructure, could enable a material to exhibit "negative" poroelasticity, where the gradient of fluid flow is opposite of a normal poroelastic material, such that the fluid flows towards the externally applied stress.

Conclusions

We have demonstrated the ability to direct and control fluid flow within a microstructured device by adjusting the microfluidic architecture. The general experimental and theoretical framework provides new capabilities for directed fluid flow using internally controlled structural deformations. By taking advantage of the inherent flexibility of typical microfluidic devices, advances can be made in microchannels for *in situ* mixing, chemical reactions, or rapid, portable chemical analysis. Additionally, proper tuning of material properties will allow directed fluid flow to be actuated by a variety of triggers, including electrical, thermal, and osmotic actuation.

Materials and methods

Experimental

The device consists of three parts: substrate, superstrate, and a thin film in between (Fig. 1); each was fabricated with polydimethylsiloxane (PDMS) (Dow Corning Sylgard 184™) mixed at a 20 : 1 ratio of prepolymer to crosslinker, and degassed in a vacuum chamber. This mixture was then molded against a glass template of a channel to form the substrate and superstrate while the thin film was prepared by spin-coating PDMS on a Petri dish, with the spin speed and time varied to control film thickness ($h = O(50\ \mu m)$). The three parts were thermally cured in an oven at 100 °C for 45 minutes.

The substrate, with a channel of length $L_0 = O(1\ mm)$, was clamped at its edges and uniaxially stretched by length $\Delta L = O(100\ \mu m)$ in the direction orthogonal to the channel, and the thin film was bonded to it using oxygen plasma treatment (Electro-Technic BD-20AC Laboratory Corona Treater) for 30 s and incubated at 60 °C for 5 min to enhance the bond strength (Fig. 1a-i). Upon release of the uniaxial strain ($\varepsilon_0 = 0.54$), the thin film buckles to form an arch of height $\tilde{w}(x)$ along the length of the channel (Fig. 1a-ii). We measured the deflection $w(x)$, the length between the two points of contact L, and the extensions ΔL using an optical microscope (Leica DMI4000 B). Finally, the superstrate was bonded to the other side of the thin film using same oxygen plasma procedure in a way that the buckled film closes the top channel (Fig. 1a-iii). The two ends of the arch orthogonal to the length of the fluid channel were sealed using PDMS, and the width of the arch D in the z direction was chosen to be greater than the arch length ($D/L \gg 1$) in order to reduce the effect of boundaries on the shape of the arch.

For the flow rate experiments, we made inlet and outlet holes in the superstrate layer with a biopsy punch. To create a pressure drop ΔP from $-L/2$ to $L/2$, the inlet was connected to a water source at a fixed height ($1\ mm \leq H \leq 10\ mm$) controlled by a vertical micrometer. This generates a pressure drop across the entire channel of $10\ Pa \leq \Delta P \leq 100\ Pa$. Since precise measurement of the pressure drop across the flexible arch was unknown, we calculated the flow rate at a constant ΔP relative to an open channel, *i.e.* Q/Q_c where Q_c refers to $b/W = 1$. We determined the flow rate Q by measuring the weight of the water at the outlet as a function of time. Numerical simulations described below show negligible differences in flow rate over this range of pressure drops. Based on the channel dimensions and measured flow rate, the Reynolds number in these experiments was $\mathscr{R} \approx 0.1$–1. The range of experimental data was limited to small values of b/W because of the stiffness of the device (Fig. 2a).

Since this buckled arch is embedded within a microfluidic device, there is a finite volume below the arch defined by the channel depth d. The ratio of final volume to initial volume cannot be neglected as this leads to a change in pressure below the arch that is enough to significantly deform the arch, and change the gap within the channel. The final pressure P_f compared to the initial atmospheric pressure P_{atm} was calculated by a simple integration of the geometry before and after fabrication, in conjunction with the ideal gas law. We chose the strain during fabrication to be $\Delta L/L \approx 0.5$ with $d/L \approx 1$ for the devices

described in this paper, as these values correspond to $P_f/P_{atm} \approx 1.15$, which will have a negligible effect on the arch's shape.

Numerical analysis

The channel was modeled in COMSOL 4.2 with the geometry and boundary conditions identical to the experimental conditions within the fabricated microfluidic device. The channel was assumed to be filled with water at the beginning while the flow was driven by a constant pressure of $\Delta P = 10$ Pa and $\Delta P = 100$ Pa. The deformation of the arch was neglected. We used the Navier–Stokes equation in its full form for incompressible flow to include the role of inertial effects as the valves open and the flow speeds increase.

Acknowledgements

Funding for this work was provided by the ARO MURI (#W911NF-09-1-0476). The authors acknowledge the helpful feedback from Ian Griffiths and Matthieu Roché.

References

1 T. J. Pedley and X. Y. Luo, Modelling flow and oscillations in collapsible tubes, *Theor. Comput. Fluid Dyn.*, 1998, **10**, 277–294.
2 J. B. Grotberg and O. E. Jensen, Biofluid mechanics in flexible tubes, *Annu. Rev. Fluid Mech.*, 2004, **36**, 121–147.
3 M. A. Biot, General theory of three-dimensional consolidation, *J. Appl. Phys.*, 1941, **12**, 155–164.
4 T. J. Pedley, B. S. Brook and R. S. Seymour, Blood pressure and flow rate in the giraffe jugular vein, *Philos. Trans. R. Soc., B*, 1996, **351**, 855–866.
5 T. S. Gross, J. L. Edwards, K. J. McLeod and C. T. Rubin, Strain gradients correlate with sites of periosteal bone formation, *J. Bone Miner. Res.*, 1997, **12**, 982–988.
6 S. Judex, T. S. Gross and R. F. Zernicke, Strain gradients correlate with sites of exercise-induced bone-forming surfaces in the adult skeleton, *J. Bone Miner. Res.*, 1997, **12**, 1737–1745.
7 S. P. Fritton and S. Weinbaum, Fluid and solute transport in bone: flow-induced mechanotransduction, *Annu. Rev. Fluid Mech.*, 2009, **41**, 347–374.
8 H. A. Stone, A. D. Stroock and A. Ajdari, Engineering flows in small devices, *Annu. Rev. Fluid Mech.*, 2004, **36**, 381–411.
9 T. Thorsen, S. J. Maerkl and S. R. Quake, Microfluidic large-scale integration, *Science*, 2002, **298**, 580–584.
10 D. C. Leslie, C. J. Easley, E. Seker, J. M. Karlinsey, M. Utz, M. R. Begley and J. P. Landers, Frequency-specific flow control in microfluidic circuits with passive elastomeric features, *Nat. Phys.*, 2009, **5**, 231–235.
11 W. Wu, A. DeConinck and J. A. Lewis, Omnidirectional printing of 3D microvascular networks, *Adv. Mater.*, 2011, **23**, H178–H183.
12 M. A. Burns, B. N. Johnson, S. N. Brahmasandra, K. Handique, J. R. Webster, M. Krishnan, T. S. Sammarco, P. M. Man, D. Jones, D. Heldsinger, C. H. Mastrangelo and D. T. Burke, An integrated nanoliter DNA analysis device, *Science*, 1998, **282**, 484–487.
13 P. Tabeling. *Introduction to Microfluidics*. Oxford University Press, 2005.
14 E. Berthier and D. J. Beebe, Flow rate analysis of a surface tension driven passive micropump, *Lab Chip*, 2007, **7**, 1475.
15 G. W. Scherer, J. H. Prévost and Z.-H. Wang, Bending of a poroelastic beam with lateral diffusion, *Int. J. Solids Struct.*, 2009, **46**, 3451–3462.
16 H. S. Kim and A. J. Crosby, Solvent-responsive surface *via* wrinkling instability, *Adv. Mater.*, 2011, **23**, 4188–4192.
17 G. M. Whitesides, What comes next?, *Lab Chip*, 2011, **11**, 191.
18 Y. Sun, W. M. Choi, H. Jiang, Y. Y. Huang and J. A. Rogers, Controlled buckling of semiconductor nanoribbons for stretchable electronics, *Nat. Nanotechnol.*, 2006, **1**, 201–207.
19 D. Y. Khang, H. Jiang, Y. Huang and J. A. Rogers, A stretchable form of single-crystal silicon for high-performance electronics on rubber substrates, *Science*, 2006, **311**, 208–212.
20 D. Vella, J. Bico, A. Boudaoud, B. Roman and P. M. Reis, The macroscopic delamination of thin films from elastic substrates, *Proc. Natl. Acad. Sci. U. S. A.*, 2009, **106**, 10901–10906.
21 L. J. Gibson, M. F. Ashby, G. S. Schajer and C. I. Robertson, The mechanics of two-dimensional cellular materials, *Proc. R. Soc. London, Ser. A*, 1982, **382**, 25–42.
22 L. Gibson and M. F. Ashby, The mechanics of three-dimensional cellular materials, *Proc. R. Soc. London, Ser. A*, 1982, **382**, 43–59.
23 R. F. Almgren, An isotropic three-dimensional structure with Poisson's ratio $= -1$, *J. Elasticity*, 1985, **15**, 427–430.
24 R. S. Lakes, Foam structures with a negative Poisson's Ratio, *Science*, 1987, **235**, 1038–1040.
25 K. Bertoldi, P. M. Reis, S. Willshaw and T. Mullin, Negative Poisson's ratio behavior induced by an elastic instability, *Adv. Mater.*, 2010, **22**, 361–366.
26 Z. G. Nicolaou and A. E. Motter, Mechanical metamaterials with negative compressibility transitions, *Nat. Mater.*, 2012, **11**, 608–613.